Modeling the Dispersal of the San Francisco Bay Plume over the Northern and Central California Shelf

Jian Zhou[1,2,3], Jonathan G. Izett[2], Christopher A. Edwards[2], Pierre Damien[3], Fayçal Kessouri[3,4], and James C. McWilliams[3]

[1]State Key Laboratory of Hydrology-Water Resources and Hydraulic Engineering, Hohai University, Nanjing, Jiangsu, China

[2]Department of Ocean Sciences, University of California, Santa Cruz, CA, USA

[3]Department of Atmospheric and Oceanic Sciences, University of California, Los Angeles, CA, USA

[4]Biogeochemistry Department, Southern California Coastal Water Research Project, Costa Mesa, CA, USA

Key Points:

- Three distinct dispersal pathways of San Francisco Bay plume are identified: southward, northward, and offshore
- Zone of impact of the northern plume is farther along-shore, narrower cross-shore, and vertically deeper compared to the southern branch
- Surface water typically spends less than 50 days in the Gulf of the Farallones after entering via the Golden Gate

Corresponding author: Jian Zhou, jzhou@hhu.edu.cn

Abstract

High-resolution simulations by the Regional Ocean Modeling System (ROMS) were used to investigate the dispersal of the San Francisco Bay (SFB) plume over the northern-central California continental shelf during the period of 2011 to 2012. The modeled bulk dynamics of surface currents and state variables showed many similarities to corresponding observations. After entering the Pacific Ocean through the Golden Gate, the SFB plume is dispersed across the shelf via three pathways: (i) along the southern coast towards Monterey Bay, (ii) along the northern coast towards Point Arena, and (iii) an offshore pathway restricted within the shelf break. On the two-year mean timescale, the along-shore zone of impact of the northward-dispersed plume is about 1.5 times longer than that of the southern branch. Due to the opposite surface Ekman transports induced by the northerly or southerly winds, the southern plume branch occupies a broader cross-shore extent, roughly twice as wide as the northern branch which extends roughly two times deeper due to coastal downwelling. Besides these mean characteristics, the SFB plume dispersal also shows considerable temporal variability in response to various forcings, with wind and surface-current forcing most strongly related to the dispersing direction. Applying constituent-oriented age theory, we determine that it can be as long as 50 days since the SFB plume was last in contact with SFB before being flushed away from the Gulf of the Farallones. This study sheds light on the transport and fate of SFB plume and its impact zone with implications for California's marine ecosystems.

Plain Language Summary

San Francisco Bay (SFB) is the largest estuary on the U.S. West Coast, situated in a highly urbanized region impacted by agricultural, industrial, and commercial wastes. As water exits the SFB through the narrow Golden Gate strait and meets the Pacific Ocean currents, it forms the SFB Plume: a layer of low-salinity water that advances over the denser seawater. Understanding how SFB plume and the nutrients, phytoplankton, and contaminants it contains are distributed in the coastal ocean is crucial for the ecosystem management of a network of National Marine Sanctuaries. This study uses three-dimensional realistic numerical simulations to explore the transport of SFB plume over the northern-central California continental shelf. We focus on the different pathways along which the SFB plume moves and the respective zones of impact in response to various atmospheric and oceanic forcings (e.g., wind and river discharge). A timescale analysis reveals that SFB plume is

typically flushed out of the Gulf of the Farallones within 50 days since it leaves the Golden Gate. Our study sheds light on how the anthropologically modulated SFB plume may influence the highly dynamic marine ecosystem off the U.S. West Coast, which supports one of the world's most productive fisheries.

1 Introduction

Rivers carry more than one-third of land-based precipitation to the ocean (Trenberth et al., 2007), channeling large freshwater fluxes through narrow outlets along the coast. The impact of the terrigenous material carried by the river water into ecologically sensitive coastal waters depends strongly on physical processes that transport and transform buoyant freshwater in the region around the river mouth as it merges with deeper, salty ocean waters. In particular, the dilution rates and along-shore transport rates of river-borne material are determined by a suite of processes, including stratified-shear mixing, frontal processes, geostrophic transport, and wind forcing (Whitney & Garvine, 2006; Horner-Devine et al., 2015; Basdurak et al., 2020; Xiao et al., 2021). In the coastal ocean, these discharges form river plumes, which are distinct regions where water properties and dynamics are significantly influenced by the riverine freshwater. The distinguishing dynamical feature of a river plume is the horizontal advection of freshwater from the river mouth that defines the shape and character of the plume. The associated dispersal pathway of a river plume depends on outflow angle (Garvine, 1999), wind forcing (Fong & Geyer, 2001; S. Lentz, 2004), ambient current (Fong & Geyer, 2002), and latitude (Sharples et al., 2017; Izett & Fennel, 2018a). Given the temporal variation of some forcing, freshwater pathways are often highly mobile, and the unsteady freshwater transport pathways have important ecological implications related to contaminant, larval, and nutrient transport (e.g., Cahill et al., 2008; Kessouri, McLaughlin, et al., 2020).

The San Francisco Bay (SFB) is the largest estuary on the west coast of North America. Its watershed extends from the ridgeline of the Sierra Nevada mountains to the strait of the Golden Gate. SFB has been a focus of research by the U.S. Geological Survey (USGS) since 1969 to learn how estuaries respond to hydroclimatic and human disturbances such as nutrient enrichment (Cloern et al., 2020). The formation of the SFB plume is due to mixing of coastal seawater that has entered the bay on flood tides and incoming freshwater from the Sacramento and San Joaquin Rivers, prior to returning to the ocean as the SFB plume on the ebb tide (Fram et al., 2007). The supply of coastal seawater into the bay far exceeds the

average river input, resulting in an SFB plume that has a relatively high salinity compared to a typical river plume. Upon entering coastal waters, the plume is influenced by prevailing winds and near surface currents north, west, or south over the relatively broad continental shelf (S. J. Lentz, 1987). The chemical constituents of the SFB plume differ from the river and coastal seawater entering the bay because the saline estuary has its own internal cycling of nutrients that is largely driven by anthropogenic inputs within the estuary (Cloern, 1996; Wang et al., 2020). Characterizing the plume's dispersal is of fundamental importance for understanding any influence of San Francisco Bay on coastal biogeochemical processes in an ecologically sensitive region (Chin et al., 2001) that includes a network of National Marine Sanctuaries (NMSs) such as the Greater Farallones NMS, the Cordell Bank NMS, and the Monterey Bay NMS. The Gulf of the Farallones is loosely indicated in Figure 3, covering the region on the shelf from Point Reyes in the north to Pedro Point south of the Golden Gate, though the boundaries of the NMS extend further north. For a map of the NMSs outside the Golden Gate, please refer to `https://farallones.noaa.gov/gallery/maps.html`. Further place names used in the text are highlighted in Figure 12.

The SFB plume enters into the California Current System (CCS), an Eastern Boundary Upwelling System (Huyer, 1983; Hickey, 1998; Jacox et al., 2018; Renault et al., 2020). In the central portion of the CCS during spring/summer, predominantly equatorward, along-shore winds induce offshore Ekman transport and coastal upwelling, drawing nutrient-rich water from depth; downwelling is driven by poleward along-shore winds that result in onshore Ekman transport (e.g., Marchesiello et al., 2003). To date, little is known about the levels and spatio-temporal patterns of SFB plume dispersal within the Gulf of Farallones and further afield in the context of complex oceanic circulations along the U. S. West Coast (Kaplan & Largier, 2006; Hurst & Bruland, 2008). As such, the mechanisms that drive SFB plume dispersal on the shelf and its subsequent fate in the coastal ocean remains unclear. Furthermore, the SFB plume has high levels of nutrients, phytoplankton, dissolved organic matter, and contaminants (Wang et al., 2020), which may be similar to upwelled concentrations (Hurst & Bruland, 2008).

In this study, we numerically investigate the dispersal pathways of the SFB plume over the northern and central California shelf in the period of 2011–2012. A downscaled Regional Ocean Modeling System (ROMS) configuration was established, scaling from a 4-km horizontal resolution configuration spanning the entire CCS (Renault et al., 2020; Deutsch et al., 2020), to a 1-km resolution grid covering much of the California coast (Kessouri, Bianchi,

et al., 2020), and finally to a 0.3-km grid along the portions of the northern and central California coast centered around the San Francisco Bay (this study). The 0.3-km ROMS grid was coupled with high-frequency ocean-estuary exchanges derived from a well-validated SFB-focused modeling study (Wang et al., 2020) using the Semi-implicit Cross-scale Hydroscience Integrated System Model (SCHISM). The main objectives are to characterize the shelf-wide spreading of SFB-sourced water discharged from the Golden Gate, and to describe the mean characteristics and temporal variability of its dispersal pathways. We will address the following two major concerns regarding the spatio-temporal pattern of the SFB plume dispersal: (i) how is the net baywater effluent dispersed in the coastal ocean along the various pathways? and (ii) how sustained are periods dominated by any given pathway throughout the investigated time span? This paper lays groundwork for coupled physical-biogeochemical investigations of anthropogenic nutrient discharges in support of San Francisco Bay Nutrient Management Strategy (`https://sfbaynutrients.sfei.org/books/nutrient-management-strategy-san-francisco-bay`).

2 Model Configuration

2.1 Oceanic Configuration

The Regional Ocean Modeling System, ROMS (Shchepetkin & McWilliams, 2005; Shchepetkin, 2015), is used for the ocean circulation simulations. ROMS is a primitive-equation, hydrostatic, terrain-following oceanic model that allows high-resolution simulations in shallow shelf seas. It contains state-of-art numerical algorithms that provide an accurate and stable representation of physical processes down to scales of tens of meters, and allows for multi-level offline downscaling of higher-resolution subdomains within larger domains. Vertical mixing in the boundary layers is represented by a K-profile parameterization (Large et al., 1994).

The U.S. hindcast model (Figure 1*a*) has been successfully run over two decades at 4-km (L0 domain) and 1-km (L1 domain) horizontal resolutions using high-resolution spatial and temporal atmospheric forcing that represents the effects of near-coast wind stress changes, current feedback on the surface stress, and high-frequency wind fluctuations (Renault, Hall, & McWilliams, 2016; Renault, Molemaker, et al., 2016). The L0 simulation was initialized and forced at the open boundaries by a pre-existing northeast Pacific-wide ROMS solution at 12-km resolution (Renault et al., 2020), which was initialized and forced on the boundaries

by the global model Mercator Glorys2V3 (`http://www.myocean.eu`). The L0 simulation was run for the period 1995-2017 after a spin-up of 2 years. The L1 simulation was then initialized and forced by the L0 model, starting in October 1996 and ending in December 2017. Readers are referred to Renault et al. (2020), Deutsch et al. (2020), and Kessouri, Bianchi, et al. (2020) for the details of 1-km and 4-km model setups and boundary forcings.

Forced at the western, southern, and northern boundaries and initialized by the L1 solution, this study investigates the L2 domain with a nominal resolution of 0.3 km (450×1200 horizontal cells in total) to capture submesoscale processes, focusing on portions of the northern and central California coast centered around the San Francisco Bay (Figure 1*a*). The offline downscaling is based on the Orlanski scheme for the baroclinic mode (Marchesiello et al., 2001) and a modified Flather scheme for the barotropic mode (Mason et al., 2010). The model domain extends along a 400-km stretch of the coast (spanning from Ragged Point in the south to Point Arena in the north), and about 150 km offshore. The bathymetry data were acquired from the General Bathymetric Chart of the Oceans (GEBCO_2019) with 15 arc-second resolution. The grid has 60 σ-coordinate vertical levels with stretching parameters of $\theta_s = 6$, $\theta_b = 3$, and $h_c = 250$ m (Shchepetkin & McWilliams, 2009). The L2 domain is tidally forced by adding the TPXO9-atlas barotropic tides (Egbert & Erofeeva, 2002) to the L1 forcing at the northern, western, and southern boudaries. The first 10 constituents are phased with the tide-resolving eastern boundary forcing from the SCHISM model (i.e., at the Golden Gate).

2.2 Ocean-Estuary Coupling

A portion of the eastern boundary of the L2 domain is forced at the Golden Gate by high-frequency (two-hourly) output from a well-validated SFB-focused modeling study over the 10-year period of 2005–2014 (Wang et al., 2020, see Figure 1*b*) using the Semi-implicit Cross-scale Hydroscience Integrated System Model (SCHISM). SCHISM is an open-source community model based on unstructured grids designed for seamless simulation of three-dimensional baroclinic circulation across creek-lake-estuary-shelf-ocean scales (Y. Zhang & Baptista, 2008; Y. Zhang et al., 2016). The 3D model output of momentum, temperature, and salinity across the Golden Gate in the SCHISM model (yellow line in Figure 1*b*) were extracted and offline coupled with the ROMS model. A major challenge was that the ROMS (structured grid) and SCHISM (unstructured grid) models differ in the bathymetry across the Golden Gate due to different horizontal and vertical resolutions. Therefore, momentum

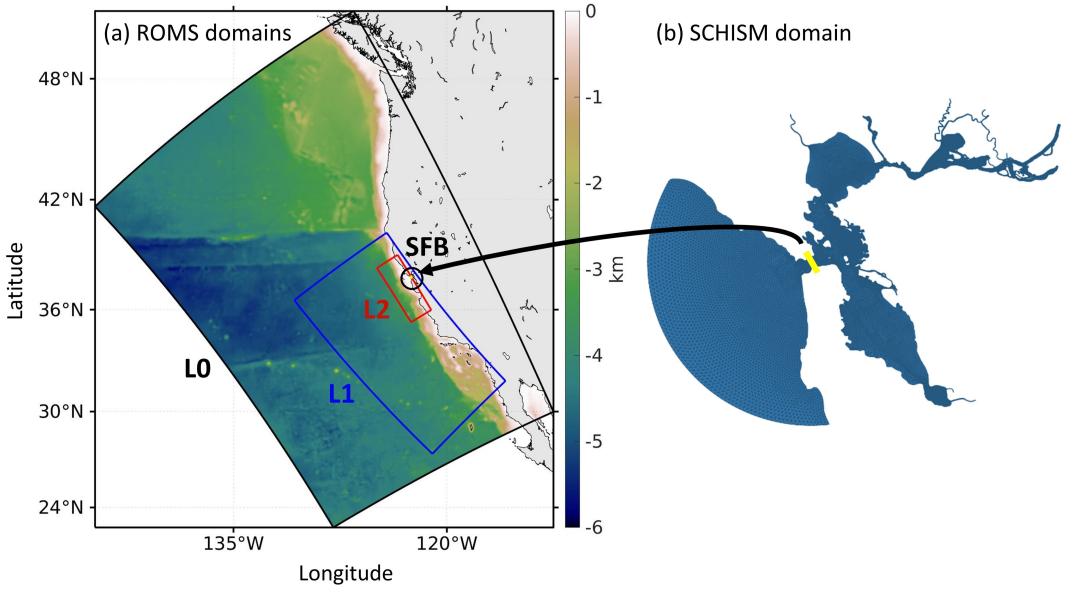

Figure 1. Model configuration: (*a*) ROMS nested domains; (*b*) SCHISM domain by Wang et al. (2020). In (*a*), continuous colors represent bathymetry along the U.S. West Coast and discrete rectangular perimeters indicate the triple grid nesting configuration. The black, blue, and red boxes show the L0, L1, and L2 domains with horizontal resolutions of 4 km, 1 km, and 0.3 km (the present study), respectively. The innermost circle in (*a*) corresponds to the estuary-focused domain in (*b*). The yellow line in (*b*) indicates the cross section from which 3D momentum, temperature, and salinity are extracted to force the eastern boundary of the L2 domain in (*a*).

and tracer concentrations were re-constructed as being laterally uniform while preserving their vertical structures, which we consider to be more important to capture the key features of ocean-estuary exchange flows at such a narrow strait. Due to the different average sea levels between models, the sea surface height at every location of the eastern boundary was forced as $\zeta = \overline{\zeta}_{\text{ROMS, no SFB-forcing}} + \zeta'_{\text{SCHISM}}$, where $\overline{\zeta}_{\text{ROMS, no SFB-forcing}}$ refers to the mean sea surface height in ROMS simulations without SFB-forcing (i.e., a closed eastern boundary condition), and ζ'_{SCHISM} represents sea surface height anomalies in the SCHISM model.

To avoid the ambiguity of reference salinity for ocean water in the coastal ocean (e.g., Castelao et al., 2008) and also to isolate the San Francisco Bay plume from other sources of fresh water in the model, a passive, conservative tracer with unit concentration was introduced at the Golden Gate. Following the simulated passive tracer concentration gives an unambiguous measure, anywhere in the model domain, of the volume fraction of water con-

tributed by the SFB outflow, hereafter referred to as "baywater". The model was initialized with zero baywater concentration everywhere outside of the Golden Gate.

As described in section 2.1, an Orlanski scheme was used for 3D temperature and salinity on the eastern boundary, while the clamped open boundary conditions was used for 3D momentum. This approach seeks discharge volume consistency with the SCHISM model, as it has been validated against measurements of major river runoffs (including Sacramento River and San Joaquin River) by the California Department of Water Resources (DWR).

The model was integrated with a baroclinic time step of $\mathrm{d}t = 30$ seconds. Model fields were saved as sequential two-hour averages in order to achieve an accurate calculation of the residual baywater flux which may be dominated by the tidal pumping flux in tidally energetic estuaries and coastal seas (Fram et al., 2007; Zhou et al., 2020; Zhou & Stacey, 2020). The L2 simulation was run from January 2011 to December 2012. Upon investigation, remnant coastal freshwater inherited from the L1 solution (where river runoff was included as surface precipitation) is completely dispersed in the L2 simulation on the order of 1–2 months, consistent with the results in section 5 where the mean water age in the Gulf of Farallones is generally less than 50 days. Given this rapid flushing, no spin-up period for the passive tracer is considered. As a verification, shifting the average time window forward by 2 months (i.e., from March 2011 to February 2013; not shown) has little effect on the long-term pattern of baywater dispersal.

3 Model Evaluation

Before proceeding to the analysis of the simulation results, we evaluate the model to establish that the modeled ocean hydrodynamics has acceptable fidelity with respect to relevant observations. We focus on the L2 domain, as the L0 and L1 domains were previously validated against available observations (Renault et al., 2020). Though discrepancies between the model and data exist, the model-data comparison for various fields shows good overall representation of features of the bulk dynamics of surface currents and state variables. Our goal is to demonstrate that the model is valid for the statistical average simulation of baywater spreading in ocean water off the central California coast. We note that there has been no assimilation of satellite or other data in these simulations.

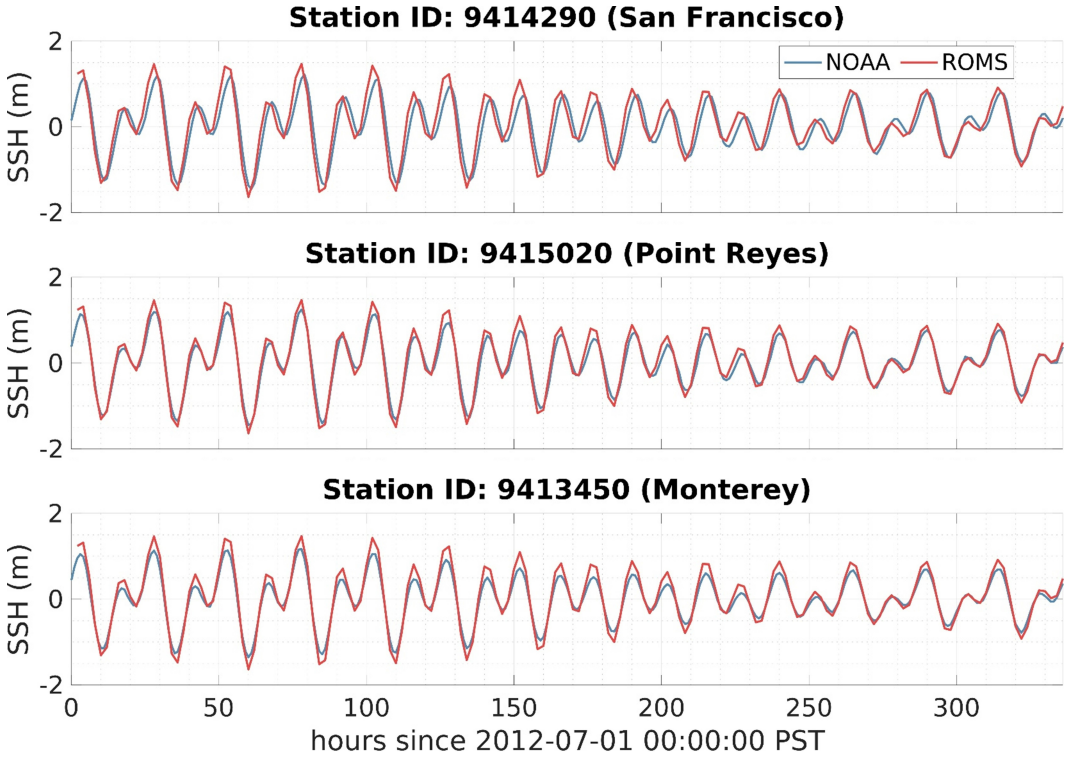

Figure 2. Comparison of modeled and observed sea surface height time-series at three representative locations (blue lines: NOAA tidal gauge measurements; red lines: ROMS simulations). Data during the first two weeks of July 2012 are shown for demonstration.

3.1 NOAA Tidal Gauge Measurements

The National Oceanic and Atmospheric Administration (NOAA) provides hourly water level information at various locations along the U.S. coast (`https://tidesandcurrents.noaa.gov/`), with three tide gauge stations within our model domain: 9414290 (San Francisco), 9415020 (Point Reyes), and 9413450 (Monterey). The modeled sea surface height is compared with NOAA measurements in Figure 2 for two weeks in July 2012. The model agrees well with the observations, with root-mean-square deviations (RMSD) between the model and observation throughout 2011–2012 of 0.318 m, 0.238 m, and 0.234 m for stations 9414290 (San Francisco), 9415020 (Point Reyes), and 9413450 (Monterey), respectively.

3.2 High-Frequency Radar Data of Surface Current

The land-based HF Radar Network (HFRNet; `https://hfrnet-tds.ucsd.edu/thredds/catalog.html`) was developed to measure the speed and direction of ocean surface currents

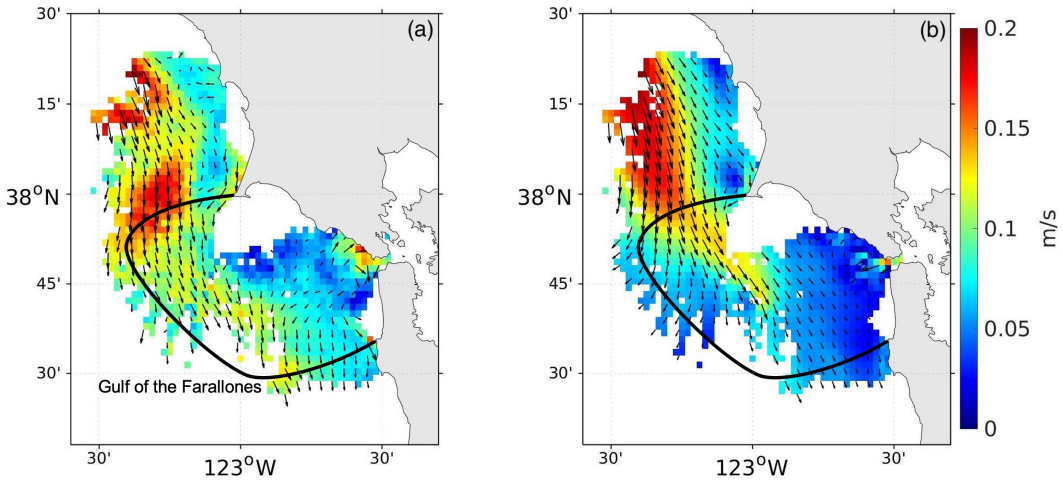

Figure 3. Comparison of annual-mean surface currents for the year 2012 at the ouflow of the Golden Gate, including the Gulf of the Farallones (indicated with black outline): (*a*) observed (HFR); (*b*) modeled. Color represents current magnitude, and scaled arrows indicate the direction. Note that the model results (0.3 km-resolution) are remapped onto the HFR grid (2 km-resolution) to aid comparison.

in near real-time. HFR data covering the U.S. West Coast (including the Central California Coast centered around the San Francisco Bay) first became available in 2012.

Figure 3 compares the annual mean surface currents between HFR data and the model in 2012. The observed data are plotted only at locations where data availability in time exceeds 70%; modeled results are plotted at the same locations for ease of comparison. Over this time period, both observations and model show a predominantly southward mean flow. Surface currents are generally weak close to the coast, strengthening offshore. A tongue-shaped zone of strong southward flow north of Point Reyes is successfully reproduced, with the model showing a somewhat more continuous pattern. Discrepancies between the model and data also exist. In particular, there exists a difference in mean flow within the Gulf of the Farallones. The model shows weak alongshore flow whereas the observations indicate stronger offshore flow. Discrepancies between observations and the model may in part result from the differing data availability across the average period: the model has full temporal coverage across the investigated period, while at some locations there are only limited HFR data available to contribute to the annual mean current. This is especially the case immediately outside of the Golden Gate where sufficiently high temporal coverage is needed to obtain averaged currents on tidal and spring-neap timescales. Meanwhile,

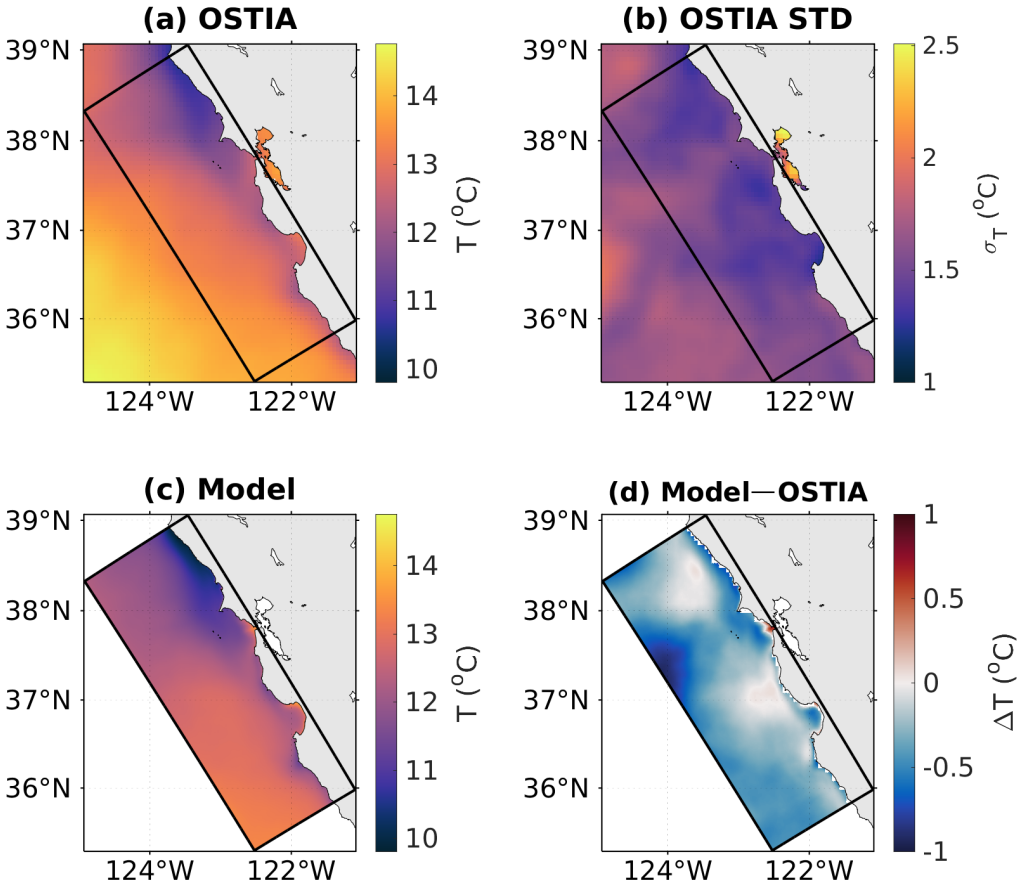

Figure 4. Comparison of observed and modeled 2-year mean sea surface temperature: (*a*) OSTIA Level-4 product; (*b*) standard deviation of OSTIA data; (*c*) modeled SST; (*d*) model bias ($\mathrm{SST}_{\mathrm{model}} - \mathrm{SST}_{\mathrm{obs}}$).

different spatial resolutions may also contribute to the model-data discrepancy (i.e. 2 km in the HFR data and 0.3 km in the model). Despite the differences, the general patterns are well represented and yield a Pearson correlation coefficient of 0.63.

3.3 Remote-Sensing Observations of Sea Surface Temperature

Sea surface temperature (SST) is one measure of ocean temperature that is readily available for model evaluation in satellite observations. We compare the GHRSST Level 4 OSTIA SST product with a spatial resolution of $0.05° \times 0.05°$ (`https://podaac.jpl.nasa.gov/dataset/OSTIA-UKMO-L4-GLOB-v2.0`) to the model results. As shown in Figure 4, the

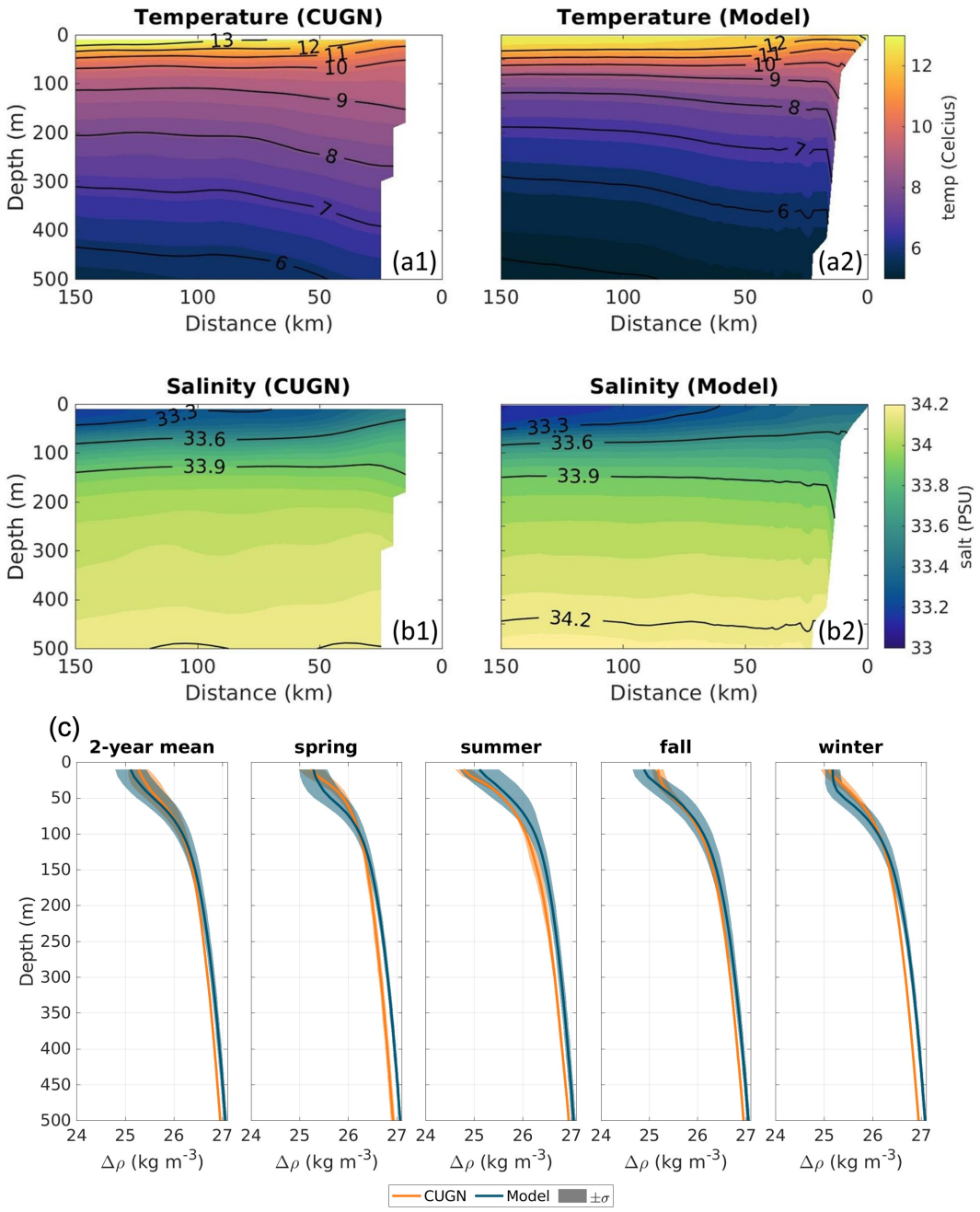

Figure 5. Model evaluation using CUGN data: (*a*) cross-shore contours of two-year mean (2011–2012) water temperature; (*b*) cross-shore contours of two-year mean (2011–2012) salinity; (*c*) vertical profiles of the density anomaly along CalCOFI line 66.7 over the entire 2-year period of 2011–2012 and in different seasons. In (*c*), both the CUGN data (orange lines) and model results (blue lines) are averaged along the cross-shore direction as shown in (*a*) and (*b*), with the sharing representing ± 1 standard deviation.

overall level and the horizontal distribution of mean SST during 2011–2012 are reasonably captured with a predominantly cold bias throughout the domain, except at the Golden Gate where modeled SST is warmer than OSTIA SST. Overall, biases are smaller than 1°C in magnitude, which is less than the OSTIA standard deviation throughout the domain. We note that instantaneous comparisons of modeled and remotely sensed SST are more variable. Greater discrepancies between model and data on short time-scales are to be expected as small-scale features (e.g., eddies and filaments) are quite nonlinear and less predictable than longer-term mean features.

3.4 The California Underwater Glider Network

The California Underwater Glider Network (`http://spraydata.ucsd.edu/climCUGN/`), CUGN, uses autonomous underwater gliders to measure variables including temperature and salinity. The gliders make repeated dives from the surface to 500-m depth and back, repeating the cycle every 3 hours, and traveling 3 km horizontally each cycle. We compare our model output to the glider data from the cross-shore California Cooperative Oceanic Fisheries Investigations (CalCOFI) line 66.7 off Monterey Bay (see black dotted line in Figure 6). For ease of comparison, both the CUGN and model data are averaged along the cross-shore direction to obtain vertical density profiles as a function of time. This comparison provides an assessment of the model performance in terms of vertical stratification in the ocean. As shown in Figure 5, agreement in the vertical structure is generally good for the two-year mean of temperature and salinity, with the mean halocline a bit deeper in the model than observations. The model successfully reproduces the shoaling of the pycnocline during summer due to solar heating and upwelling, while also capturing the deepening during winter due to diminished insolation and increased surface turbulence (Figure 5*c*). The modeled mean pycnocline is, however, deeper (∼10 m) than observed in spring and winter, with less (more) dense surface water in fall (summer).

4 Baywater Dispersal

4.1 Analysis Framework

To examine the patterns of the SFB plume spreading over the continental shelf and beyond, we consider flow across a total of 30 arcs (thick gray lines in Figure 6) centered at the Golden Gate. The radii of the arcs increase by 5 km, starting at a radius of 5 km

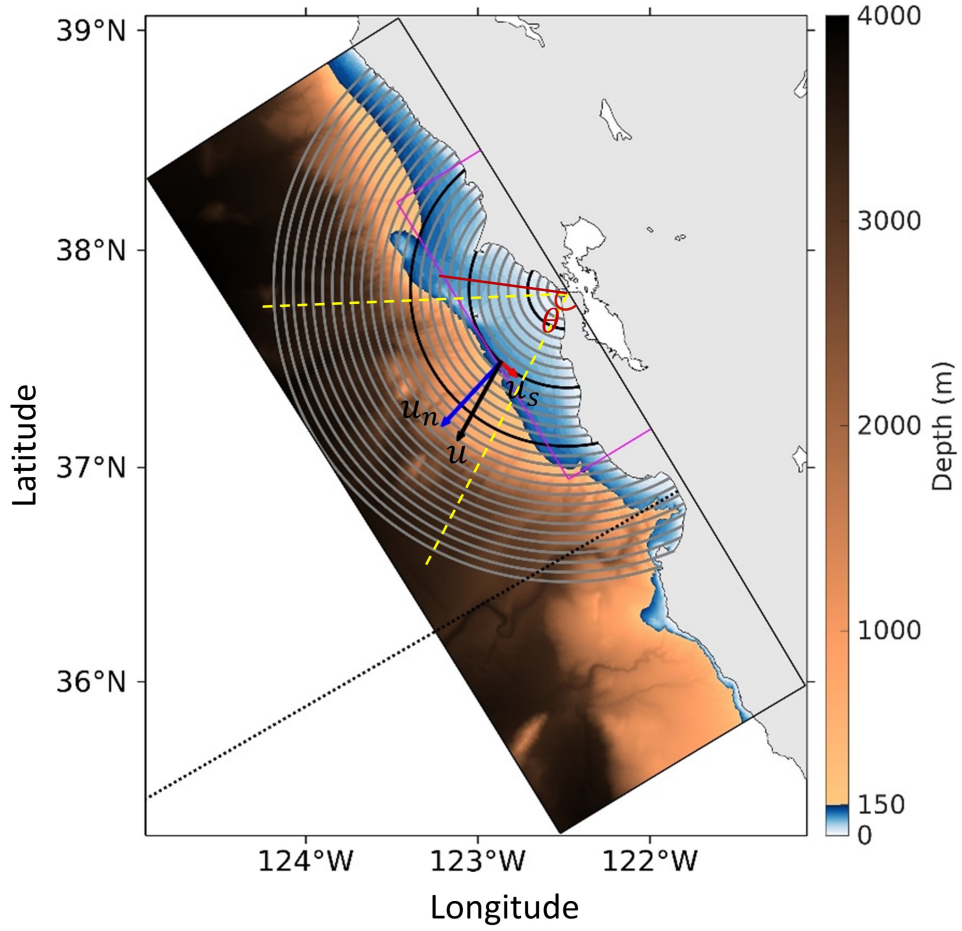

Figure 6. Analysis framework of baywater dispersal superimposed on the bathymetry of the present L2 domain. The continental shelf (defined as regions with depths $\leq$ 150 m) is highlighted by the bluish colorscale. The concentric arcs on which passive tracer flux is calculated are colored by gray, except for the three black arcs which indicate the locations of the representative arcs in Figure 8. The azimuth angle θ starts at the eastern edge of the grid and increases clockwise. The yellow dashed lines divide the arcs into their southern, offshore, and northern segments (as θ increases from zero). The magenta box indicates the subdomain within which the winds and surface currents are averaged in Figure 10. The CalCOFI line 66.7 is marked by the black dotted line (see section 3.4).

(arc 1) out to a radius of 150 km (arc 30). Throughout this paper, "arc i" corresponds to the arc with a radius of $5i$ km. At any location on a certain arc, the flow velocity vector is decomposed into its normal component u_n (blue arrow) and tangential component u_s (red arrow). Positive u_n is defined as outgoing from the source (i.e., spreading away from the

SFB), and positive u_s indicates velocities directed toward the northern end of an arc. We focus primarily on arcs with radii smaller than 100 km.

4.2 Mean Plume Characteristics

The two-year (2011-2012) time-averaged, depth-integrated passive-tracer concentration (Figure 7a) reveals the typical patterns of the SFB plume as it disperses across the northern and central California shelf. For visualization, the color scale for the depth-integrated tracer C_{VI} is selected to have an upper limit of 1 in order to emphasize tracer decay structure over the shelf. The immediate inner-shelf region within the first arc is heavily influenced by the tidal jets through the narrow Golden Gate, exhibiting elevated levels of vertically integrated tracer ranging from 1–30. Throughout much of the domain, except for the tidally dominated region < 25 km from the Golden Gate, the standard deviation of the mean field (Figure 7b) is considerably larger than the mean, highlighting the plume's variability. Overall, the plume influences a large region of the shelf, with the mean tracer found all along the shelf from near Point Arena to the Monterey Bay.

In addition to horizontal variability, the plume is vertically inhomogeneous. Figure 7c plots the mean centroid depth the SFB plume, $h_c = \int zC\mathrm{d}z / \int C\mathrm{d}z$. Overall, the plume centroid remains shallower than ~ 20 m deep throughout much of the Gulf and to the south, with plume waters north of Point Reyes extending more deeply. On the innermost arcs, the plume occupies the whole water depth ($D < 2h_c$). As the arc crosses the shelf break (around r = 50 km), depth increases dramatically and $2h_c$ more reasonably represents the vertical plume dimension.

The 2012 monthly mean fields in Figures 7d–o further illustrate the temporal variability of the plume, with the spatial pattern highly variable. Three major baywater transport pathways emerge: (i) a northward pathway, (ii) a southward pathway, and (iii) an offshore-directed pathway. The northward pathway is characterized by a sharp, buoyant coastal current whose tracer signature extends well north of Point Reyes to roughly 120 km up the coast, largely penetrating deeper than the rest of the plume and travelling closer to the coast. The second pathway is directed southward from the Golden Gate. It starts as a strong, broad, shallow feature near its source (r$<$ 20 km) that is roughly twice as wide and the northward pathway and with the highest concentrations shifted offshore. The plume becomes increasingly diffuse and less concentrated between 30 and 100 km from the Gate. The

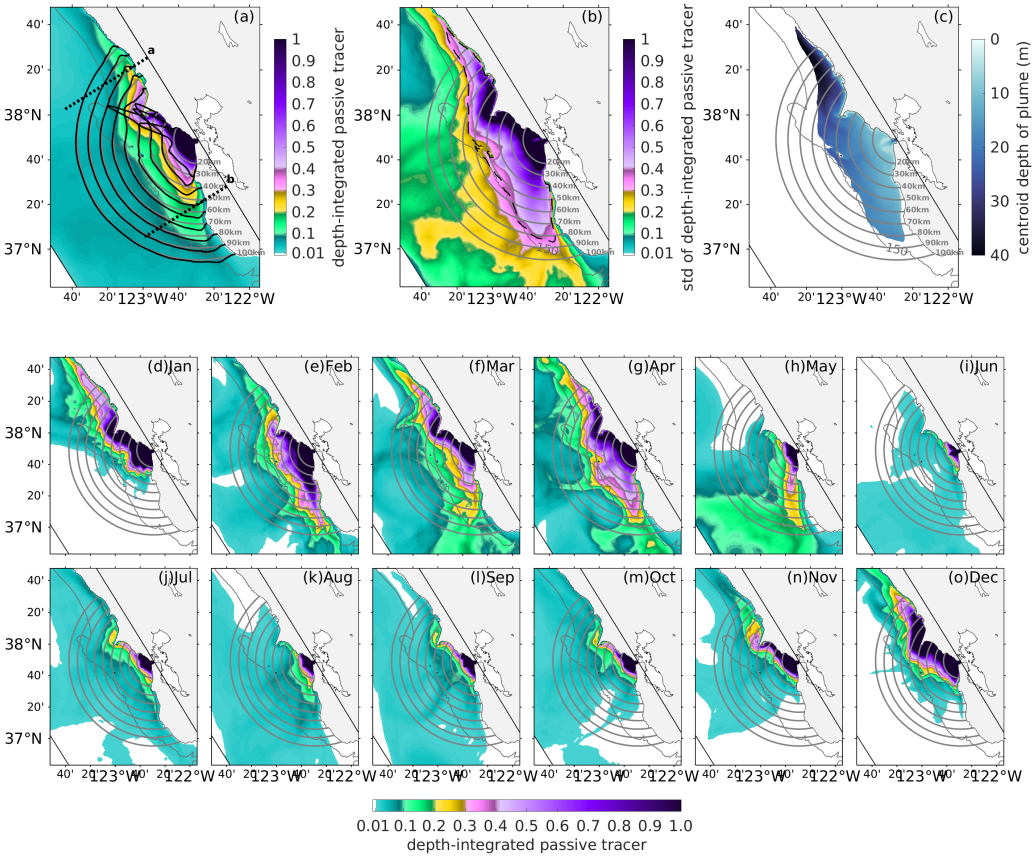

Figure 7. Depth-integrated passive tracer. (a) Two-year mean vertically integrated passive tracer concentration, C_{VI}. Black lines indicate the vertically integrated tracer flux across each arc. The two dotted lines indicate locations of the cross-shore planes in Figure 11 that extend 80 km from the eastern edge of the domain. (b) Standard deviation of mean passive tracer with dashed line indicating the point where $C_{VI} = 0.1$ in (a). (c) Centroid depth of passive tracer within the mean plume. (d–o) Monthly mean vertically integrated tracer concentrations in the year 2012. In all panels, the 150-m isobath is shown as a demarcation between shelf and slope.

third pathway is directed westward, but decays offshore quite rapidly, extending only weakly beyond the shelf-break. This pathway appears transiently and rarely in instantaneous fields compared to the northward and southward directed motions.

The cross-shelf dispersal of baywater seems to be greatly suppressed, with the majority of the SFB plume body (e.g., with depth-integrated passive tracer concentrations higher than 0.1) largely inshore of the 150-m isobath (see the portion of plume encompassed by the dashed line in Figure 7*b*). Conservation of potential vorticity in a rotating, homogeneous, in-

329 viscid, and steady fluid requires transport along and not across bathymetric contours (Brink,
330 1998). Though this fluid is not homogeneous, inviscid, or steady, cross-isobath transport is
331 severely constrained in this region, as it is in other coastal environments. Although cross-
332 shore Ekman transport at the surface and in the bottom boundary layer, as well as transient
333 motions (e.g., eddies and filaments), do result in cross-shore flow, their impact on the mean
334 baywater dispersal is quite modest. While the California Current system is an eddy-rich
335 region (Kessouri, Bianchi, et al., 2020) with potential impacts on biogeochemical activity
336 (Gruber et al., 2011), our simulations do not indicate eddy transport as a significant mech-
337 anism within the Gulf of the Farallones itself. Instead, we find that the eddy kinetic energy
338 within the Gulf is almost entirely contained within sub-tidal timescales, with little sustained
339 (sub-)mesoscale energy (not shown).

340 The mean radial flux of baywater reveals vertical and horizontal plume structure at
341 different distances from the Golden Gate. Figure 8 plots azimuth-depth contours of tracer
342 flux across three representative arcs. On arc 4 (Figure 8*a*), a typical two-layer estuarine
343 circulation (gravitational circulation; Geyer & MacCready, 2014) can be observed even at
344 this offshore location, with outgoing flux near the surface and ingoing flux at depth. On arc
345 10 (Figure 8*b*), the estuarine circulation largely diminishes, and there exists an ingoing flux
346 between $\theta = 100$–$150°$, associated with a recirculation near Drakes Bay and south of Point
347 Reyes (see Figure 7*a*). On arc 16 (Figure 8*c*), the bathymetry deepens significantly as the
348 arc crosses the shelf break. At this distance, it is clear that the plume exists as a thin layer
349 in the upper few tens of meters, sharply differentiated from the underlying shelf and slope
350 water. This structure is a common feature of surface-trapped river plumes (Fong & Geyer,
351 2002; Horner-Devine et al., 2015).

352 A more quantitative description of the average baywater dispersal can be based on
353 simple geometrical arguments, testing a model to describe the mean vertically integrated
354 passive tracer concentration ($\overline{C}_{VI}$) on a given arc, knowing only the modeled vertically
355 integrated passive tracer concentration on arc 1 ($\overline{C}_{VI,\text{modeled}}\Big|_{r_1}$). The overbar here indicates
356 averaging along a given arc (i.e., arc-averaged). The total concentration along an arc of
357 radius, r, is equal to $2\pi\overline{C}_{VI,\text{calculated}} \cdot r$. If we assume that all of the passive tracer on arc 1
358 is dispersed onto an outer arc, a uniformly spreading plume would be described as

$$\overline{C}_{VI,\text{calculated}} = \overline{C}_{VI,\text{modeled}}\Big|_{r_1} \cdot (r/r_1)^{-1} \,. \tag{1}$$

359

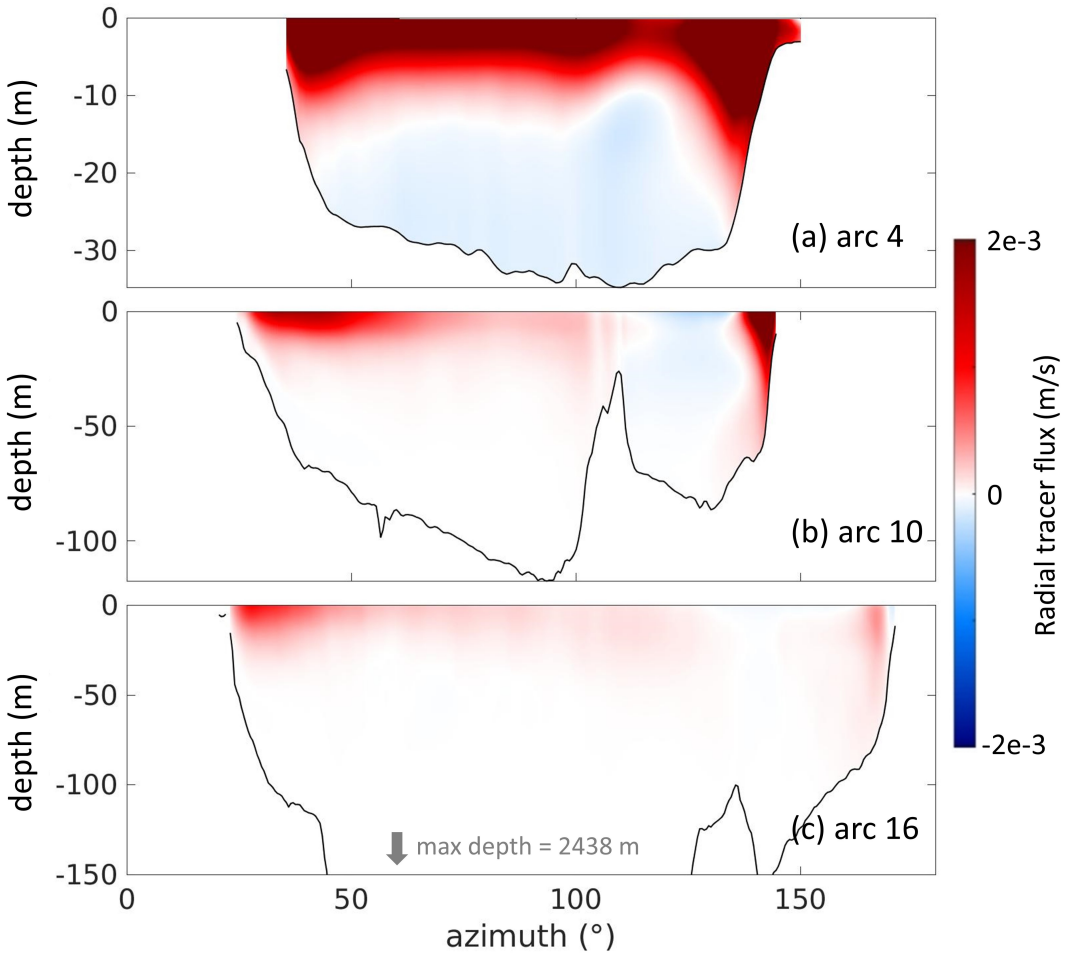

Figure 8. Two-year mean radial tracer flux across three representative arcs. Note the differing extents of vertical axes among panels. In (*c*), the max depth reaches 2438 meters, but only the upper 150 meters of water is shown.

Equation (1) is plotted in Figure 9 for all the 30 arcs considered in section 4.1. Rather than scaling directly with the ratio of the arc radii, the plume is best described by a -1.4 power law, a more rapid decline in concentration than predicted by pure spreading. The -1.4 power relationship likely results from the local storage of tracer on the inner arcs and cross-arc mixing. It is also worth noting that as r increases in Figure 9, the curve of $2\overline{h}_c$ (an approximation for the arc-averaged vertical dimension of the plume) gradually flattens, in contrast to the considerable increase of arc-averaged water depth $\overline{D}$. This is consistent with Figure 8*c* where the plume exists as a thin surface layer on distant outer arcs.

The above spreading analysis assumes advective dispersal. A similar exercise can also be conducted for a purely diffusive case. Assuming a continuous point source at the origin,

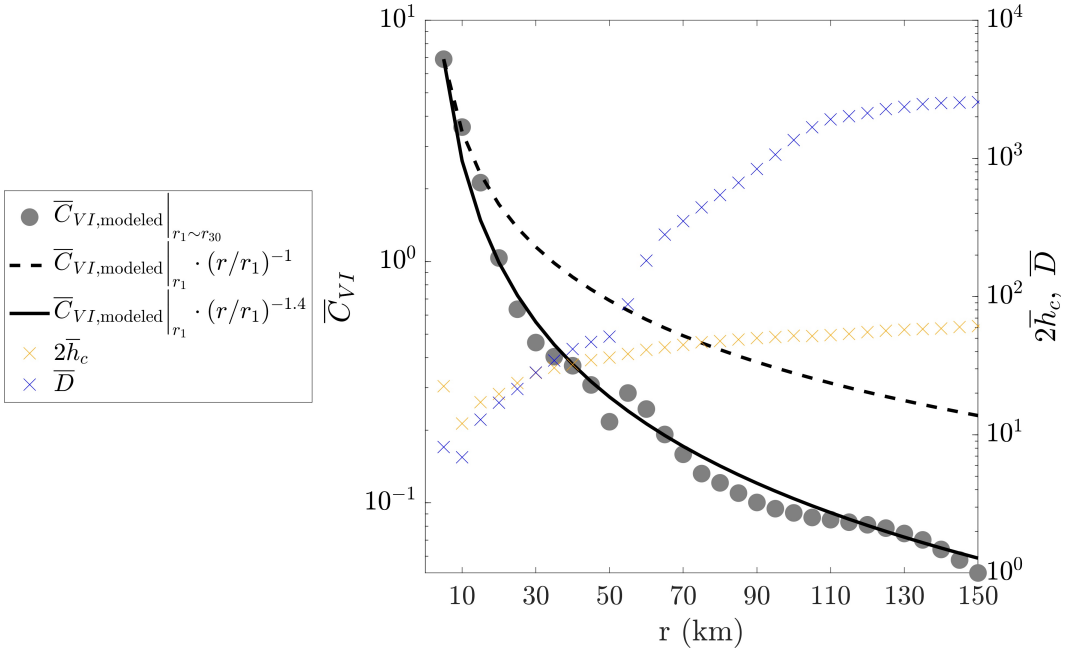

Figure 9. Vertically integrated passive tracer averaged along a given arc, $\overline{C}_{VI}$, as a function of arc radius, illustrating the geometrical plume spreading.

if the diffusion coefficient is κ and the source strength at radius $r = 0$ is $S > 0$ starting at $t = 0$ when the concentration is $C(r, 0) = 0$, then the concentration on each arc will increase in time and decrease with distance according to (Carslaw & Jaeger, 1959; Crank, 1975):

$$C\left(r,t\right) = \frac{S}{4\pi\kappa} E_1\left(\frac{r^2}{4\kappa t}\right), \tag{2}$$

where $E_1\left(x\right) = \int_x^\infty \frac{e^t}{t} dt$ is the exponential integral. Under this purely diffusive assumption, the concentration decreases rapidly with increasing radial distance. Combining both the advective and diffusive analysis, we cam infer that the transport is predominantly advective, though with some diffusive influence and storage given the more rapid decay in concentration ($r^{-1.4}$) than predicted by pure advection.

4.3 Drivers of Temporal Variability

While mean properties are useful to describe the overall behavior of the SFB plume, temporal information offers understanding of the drivers of plume dynamics. Two-year timeseries of several fields related to baywater dispersal are presented in Figure 10, including the net baywater discharge at the Golden Gate, the cross-shore and along-shore winds, the along-shore barotropic pressure gradient, and the along-shore surface-current velocity.

We note that the net baywater discharge in Figure 10*a* should not be interpreted as the conventional "river discharge" of typical river plumes because freshwater enters the San Francisco Bay from the Sacramento River and San Joaquin delta far upstream of the Golden Gate, and these waters undergo intensive mixing with saline water of coastal origin before being exported from the estuary. To remove high-frequency signals and focus on subtidal frequencies, we apply a Godin filter, a three-step low-pass filter (Godin, 1972), to all time-series in this figure. Despite this filtering, there remains a small spring-neap cycle visible in Figure 10*a* that likely still results from tidal aliasing. Winds and surface currents are spatial averages within a sizable subdomain (indicated by the magenta box in Figure 6) that spans the majority of the region of interest. Positive baywater flux is defined as outgoing from SFB.

The bay discharge (Figure 10*a*) shows largest amplitude in the spring of 2011 with small values through the rest of the 2-year period. The winter/spring signal in Q is surprisingly muted in 2012. Characteristic equatorward winds are apparent during much of the two years (Figure 10*c*), punctuated by brief reversals (also referred to as relaxations) that last a few days except for more sustained poleward winds during early spring of 2011 and 2012 and late fall/winter of 2012. The spatial mean along-shore surface current (Figure 10*e*) generally follows that of the along-shore wind, except for September 2011–January 2012 when the Davidson Current (a poleward surface coastal current off U.S. West Coast) dominates (Reid & Schwartzlose, 1962; Hickey & Pola, 1983; Connolly et al., 2014). This is manifested by the poleward barotropic pressure gradient between September 2011 and January 2012 in Figure 10*d*.

Figure 10*f*–*h* presents plume dispersal characteristics, including net baywater discharge across arc 10 ($r = 50$ km) as a function of time and angle relative to the alongshore strike of the coast (Figure 10*f*), the total transport across arc 10 in the three pathways identified (Figure 10*g*), and the angle reached by the furthest point on the plume with a vertically integrated passive-tracer concentration of at least 1.0 (Figure 10*h*). An azimuth of 25° indicates transport adjacent to the coast south of the Golden Gate, 90° indicates the direction directly offshore, and 145° corresponds to waters adjacent to the coast to its north. Regions with azimuth ranges of 0°–25° and 145°–180° are land-masked.

Figure 10*f* reveals characteristic spatial and temporal patterns of baywater discharge. Export from the Golden Gate generally crosses arc 10 either over much of its southern

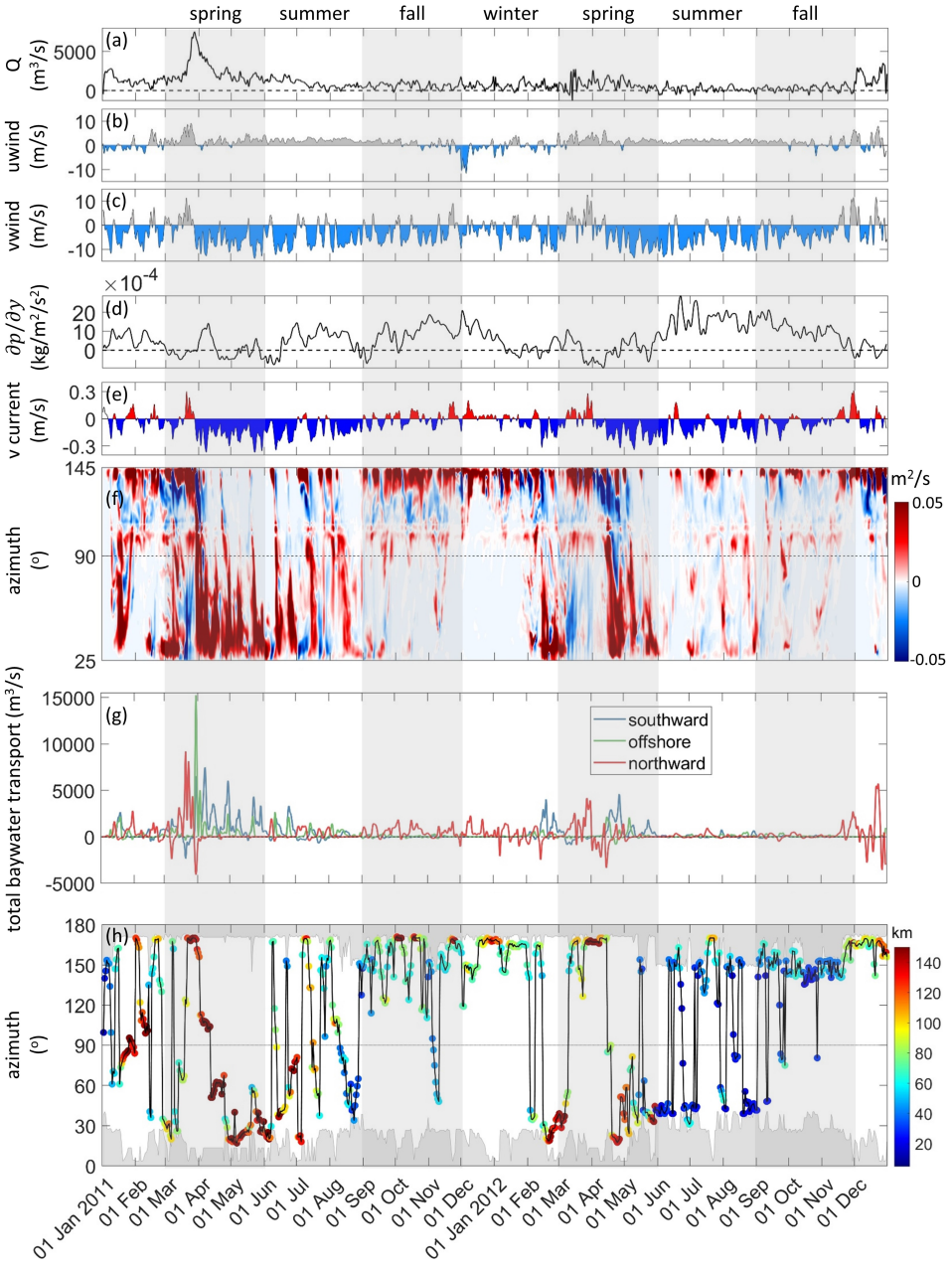

Figure 10. Godin-filtered time series of (a) net baywater discharge at the Golden Gate; (b) subdomain-averaged cross-shore wind (light blue indicates easterly wind); (c) subdomain-averaged along-shore wind (light blue indicates northerly wind); (d) along-shore barotropic pressure gradient, $(p_{\text{south}} - p_{\text{north}})/L$, in a narrow coastal band (L is the along-shore distance between the northern/southern boundaries); (e) subdomain-averaged along-shore surface current (blue indicates southward current); (f) vertically integrated baywater flux across arc 10.; (g) spatially integrated baywater transport across the three segments of arc 10; (h) positional history of the plume front. In (h): color indicates the radius of the outermost arc across which the maximum vertically-integrated tracer concentration C_{VI} is higher than 1.0; and vertical axis indicates the azimuthal location of maximum value on the outmost arc; gray-shaded area represents the coastal land-masked cells for the corresponding arc.

411 half, or in a very narrow zone near its northern edge. Between these export signals is a
412 recirculation that crosses the arc toward the Golden Gate, between $\theta \approx 105°$ and 125°,
413 consistent with the baywater circulation shown in Figure 7. All of these features of the
414 cross-arc flow variability can also be observed for arcs with $r = 20$–60 km in Figure 7, but
415 disappear for more distant arcs ($r = 70$–100 km; not shown).

416 There is a noticeable seasonality in the baywater dispersal patterns, with peak fluxes
417 predominantly occurring during spring months and the temporal variation of baywater
418 highly dependent on net input of baywater into the domain, the wind field, and the surface
419 current. Generally south and northward baywater flux occur during south and northward
420 alongshore surface currents (Figure 10*e*), respectively. The baywater transport intensity on
421 the arc differs between years, with the outgoing flux being stronger and more continuous in
422 the spring of 2011 than in 2012, and clearly related to the interannual differences in peak
423 discharge. Overall, there is a pattern of north/south switching, with baywater discharge
424 generally being larger in magnitude to the south or north but not simultaneously.

425 Consistent with idealized river plume studies (e.g., Fong & Geyer, 2001, 2002; S. Lentz,
426 2004), the pattern of the along-shore wind field significantly influences the behavior of the
427 SFB plume. As shown in Figure 11, the direction and magnitude of the wind forcing deter-
428 mines the plume shape. Southerly, downwelling-favorable wind drives northward dispersal
429 of baywater and the associated onshore surface Ekman transport confines higher concentra-
430 tions near to the coast (Figure 11*a*). Equatorward (northerly), upwelling-favorable winds
431 lead to southward dispersal of baywater and the associated offshore surface Ekman trans-
432 port draws the plume away from the coast (Figure 11*b*). These qualitative descriptions are
433 borne out in the spatial patterns shown in Figure 7.

434 A plume's trajectory is the result of its forcing history. As such, comparing instanta-
435 neous forcing to instantaneous plume direction does not result in any significant correlations.
436 We find, however, that comparing 1-week running means with lag times of up to a few days
437 can result in high correlations between a forcing parameter and plume azimuth. Azimuth
438 is most strongly related to the surface currents ($r^2 > 0.8$ for a two-week lag), which are in
439 turn strongly related to the near-surface winds. As a result, the mean plume azimuth is
440 also well-correlated with the wind direction ($r^2 > 0.7$), with strengthening northerly winds
441 resulting in more pronounced southward plume transport.

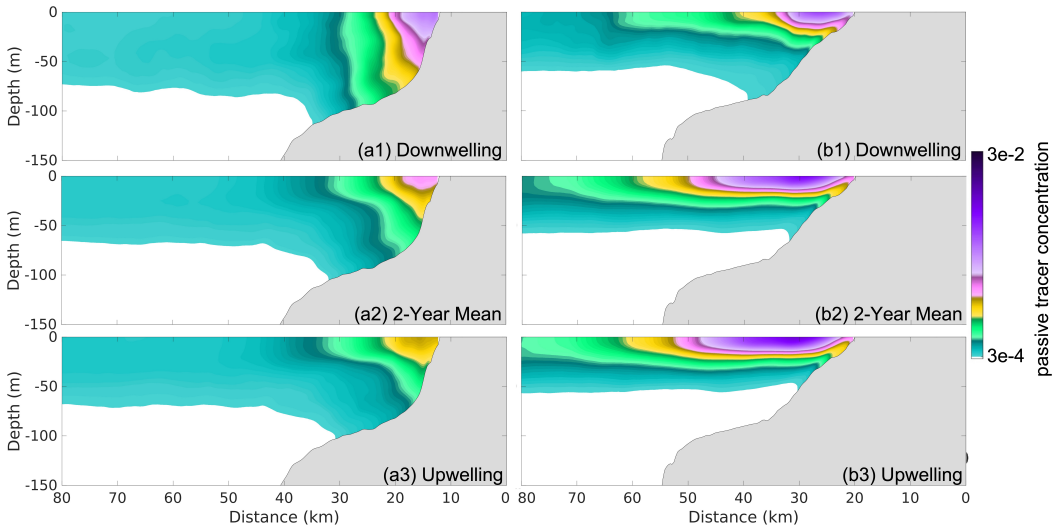

Figure 11. Cross-shore contours of passive tracer concentration at transects a and b in Figure 7a for different conditional averaging: (1) during downwelling (southerly winds) conditions, (2) two-year mean, and (3) during upwelling (northerly wind) conditions.

4.4 Spatio-Temporal Summary of Transport

Based on the discussions in preceding sections, Figure 12 provides a more global perspective on the spatio-temporal pattern of the shelf-wide spreading of the SFB plume. Figure 12 plots the total baywater transport (solid lines) and the total time spent in a given pathway (dashed lines) with increasing arc radius on the vertical axis. More precisely, $\overline{Q}_i$ is the two-year averaged, spatially integrated baywater transport across the three arc segments as defined in Figure 6, where i corresponds to one of the following: "total", "southward", "offshore", and "northward", and $\overline{Q}_{GG}$ is the two-year mean baywater discharge at the Golden Gate, which is 924 m^3 (an invariant number that is strictly matched between ROMS and SCHISM models). The total time the plume is dominated by southward, offshore, and northward baywater transport, denoted $\sum T_i$, is determined by accumulating periods with the largest intensity of the three pathways throughout 2011–2012 on each arc (see Figure 10*g* for the example of arc 10 with a radius of 50 km). Finally, $\sum T_{total}$ is the total length of the two-year timeframe.

Values for $\overline{Q}_i/\overline{Q}_{GG}$ reveal how net baywater effluent is distributed along the different transport pathways in a temporally averaged sense. For example, at $r = 75$ km, $\overline{Q}_{southward}/\overline{Q}_{GG} = 43.5\%$ (blue solid), indicating that on this arc 43.5% of the total bay-

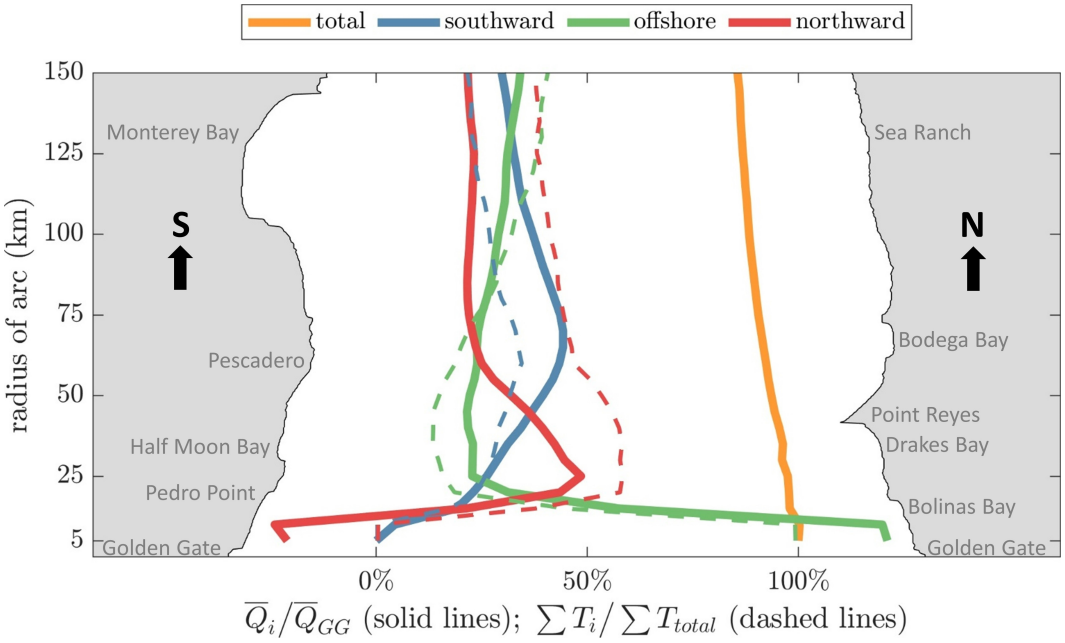

Figure 12. Spatio-temporal pattern of baywater dispersal as a function of arc radius. Solid lines: proportions of two-year mean southward (θ = 0–120°), offshore (θ = 120–240°), and northward (θ = 240–360°) transport of the total 2-year mean discharge at the Golde Gate (924 m^3); Dashed lines: fraction of time dominated by southward, offshore, and northward transport throughout 2011–2012. The southern and northern coastlines surrounding the Golden Gate are superimposed to provide context for the given radii.

water discharge is dispersed along the southward pathway. Near the Golden Gate ($r < 25$ km), offshore transport $\overline{Q}_{offshore}/\overline{Q}_{GG}$ (green) dominates other pathways and for $r < 10$ km, the northern pathway (red) is negative, indicating a return flow on northern segments. Offshore transport declines rapidly from the Golden Gate as the baywater tracer flux shifts primarily to the northern and secondarily to the southern pathways. At arcs free from the SFB tidal pulses ($r > 25$ km), $\overline{Q}_{offshore}/\overline{Q}_{GG}$ shows a mild increase as it receives tracer from two separate sources: (i) Tracer within the northward pathway shifts to the offshore pathway due to southward transport near Point Reyes ($25 < r < 50$ km) and direct advection by the prevailing northerly wind still further north ($r > 50$ km). The northward fraction, $\overline{Q}_{northward}/\overline{Q}_{GG}$, shows a corresponding decrease for $25 < r < 70$ km; (ii) The offshore pathway also receives offshore-advected water from the southward pathway due to surface Ekman transport and possibly from the transient, directly offshore motion. This is accompanied by the decrease of $\overline{Q}_{southward}/\overline{Q}_{GG}$ for $70 < r < 150$ km. Comparing vari-

ations of $\overline{Q}_{northward}/\overline{Q}_{GG}$ and $\overline{Q}_{southward}/\overline{Q}_{GG}$ for $50 < r < 70$ km reveals that much of the water originally along the northward pathway is ultimately passed on to the southward pathway, with the offshore third acting as a mediator. The fact that there is no noticeable increase in the offshore transport at this distance is indicative of the tracer passing through the arcs with no flux divergence in and out of the region. The sum-total baywater transport $\overline{Q}_{total}/\overline{Q}_{GG}$ (yellow) gradually decreases towards outer arcs due to small local storage of tracer in areas between the inner arcs over this two year period.

The ratio of $\sum T_i/\sum T_{total}$ (dashed lines in Figure 12) reveals how dominant each pathway is through the modeled period and comparing $\sum T_i/\sum T_{total}$ to $\overline{Q}_i/\overline{Q}_{GG}$ reveals information about the intensity of transport. For example, the fraction of southward transport, $\overline{Q}_{southward}/\overline{Q}_{GG}$ always exceeds the fraction of time the plume is dominated by southward transport, $\sum T_{southward}/\sum T_{total}$. This means that the southward pathway accounts for a larger portion of the total baywater transport in less time. In contrast, $\overline{Q}_{northward}/\overline{Q}_{GG}$ is always less than $\sum T_{northward}/\sum T_{total}$ meaning that the more frequent northward pathway accounted for less transport of plume water over the two-year period. This imbalance in transport is likely due to the coincidence of peak discharge and persistent northerly wind in Spring of 2011 (Figure 10), rather than an indication that the southward transport is somehow more efficient. The offshore pathway, having strong interaction with the two alongshore pathways, exhibits an intermediate state with a transition point $r \simeq 80$ km (where the solid and dashed green lines intersect). Performing an average across all the 30 arcs, weighted by arc radius, we are able to give the following estimates of the spatio-temporal pattern of SFB plume dispersal during 2011–2012: (i) of the two-year mean net discharge of 924 m^3, 11.1% is stored within 150 km of the Golden Gate, 35.1% is dispersed southward, 29.7% is dispersed offshore (up to the shelf break), and 24.1% is dispersed northward; (ii) across the two-year time span, the discharged baywater is dispersed southward for 26.0% of the time, offshore for 31.8% of the time, and northward for 42.2% of the time.

5 Water Age

Water age has utility for estimating ventilation rates of ocean basins, inferring ocean circulation and mixing, and studying rates of biogeochemical processes (W. G. Zhang et al., 2010). In this section, we focus on the time scale associated with the spreading of the SFB plume over the northern and central California shelf. We apply the constituent-oriented age theory (Delhez et al., 1999) to the circulation of the SFB-sourced water.

5.1 The Constituent-Oriented Age Theory

According to the constituent-oriented age theory (Delhez et al., 1999), the age of a passive tracer is a time-dependent, pointwise quantity that can be obtained from the solution of two partial differential equations governing the evolution of the concentration of the passive tracer (C) and an auxiliary variable called the "mean age concentration" (α).

In this approach, each fluid parcel at position $\boldsymbol{x}$ and time t is recognized to consist of constituents having different ages (i.e., times since leaving the Golden Gate). A parcel's age concentration (i.e., the concentration of tracer with a particular age τ) is denoted $c(\boldsymbol{x}, t, \tau)$, where $\boldsymbol{x}$ refers to the parcel position at time t. The total passive tracer concentration is calculated as the integral of the age concentration across all ages $C(\boldsymbol{x}, t) = \int_0^\infty c(\boldsymbol{x}, t, \tau) d\tau$, and the mean age concentration $\alpha(\boldsymbol{x}, t)$ is given by the first moment of the age concentration, $\alpha(\boldsymbol{x}, t) = \int_0^\infty \tau c(\boldsymbol{x}, t, \tau) d\tau$. The mean age, $a(\boldsymbol{x}, t)$, is obtained as the ratio of the mean age concentration to the total tracer concentration,

$$a(\boldsymbol{x}, t) = \frac{\alpha(\boldsymbol{x}, t)}{C(\boldsymbol{x}, t)}. \tag{3}$$

In this application, concentration and age tracers are introduced only at the Golden Gate and there is no production or destruction of tracer within the domain. Concentrations of a given age can be changed through advection, mixing, and aging of the tracer itself. Thus, the evolution of age concentration obeys

$$\frac{\partial c}{\partial t} = \boldsymbol{\nabla} \cdot (\boldsymbol{u} c - \boldsymbol{K} \cdot \boldsymbol{\nabla} c) - \frac{\partial c}{\partial \tau}. \tag{4}$$

Here, the flow velocity is given by $\boldsymbol{u}$, and $\boldsymbol{K}$ represents the eddy diffusivity tensor. The final term on the right-hand side represents the aging of water within the grid cell.The integral of equation (4) with respect to τ yields an expression for the time evolution of $C(\boldsymbol{x}, t)$. Applying a sensible constraint on the age concentration, $\lim_{\tau \to \infty} c(t, \boldsymbol{x}, \tau) = 0$, one obtains

$$\frac{\partial C}{\partial t} = c(\boldsymbol{x}, t, \tau = 0) - \boldsymbol{\nabla} \cdot (\boldsymbol{u} C - \boldsymbol{K} \cdot \boldsymbol{\nabla} C)\,. \tag{5}$$

The evolution equation for the mean age concentration $\alpha(\boldsymbol{x}, t)$ is obtained by multiplying equation (5) by τ and integrating in τ

$$\frac{\partial \alpha}{\partial t} = C(\boldsymbol{x}, t) - \boldsymbol{\nabla} \cdot (\boldsymbol{u} \alpha - \boldsymbol{K} \cdot \boldsymbol{\nabla} \alpha)\,. \tag{6}$$

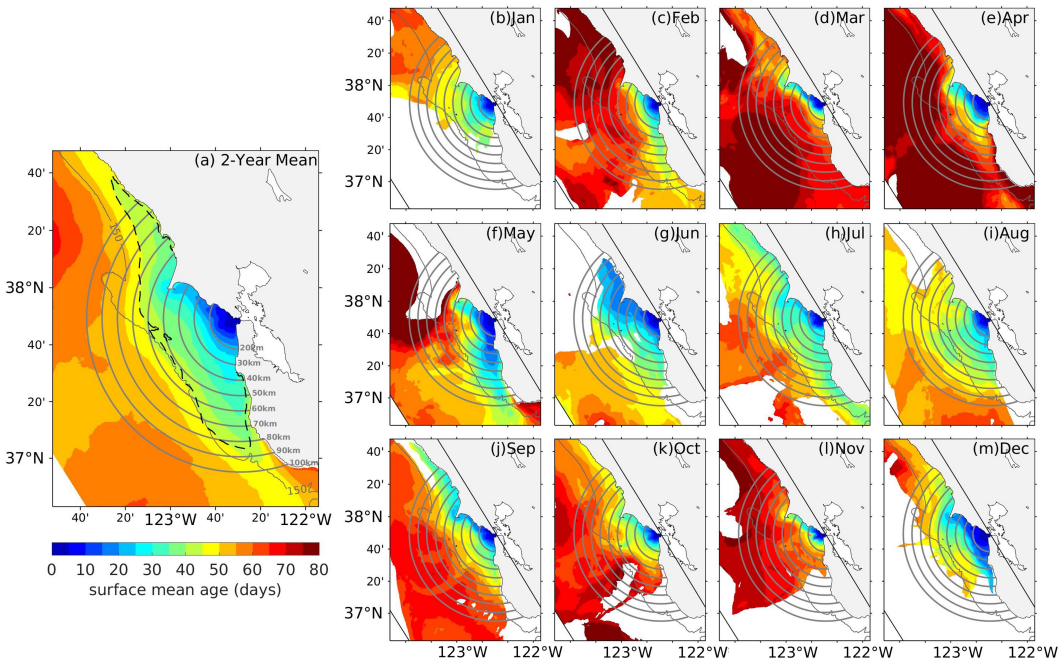

Figure 13. Surface mean age where depth-integrated passive tracer concentration $C_{VI} \geq 0.01$: (a) two-year mean; (b–m) monthly mean in the year 2012.

The total tracer concentration $C(\boldsymbol{x}, t)$ thus drives changes in mean age concentration. Considering an isolated parcel in the absence of advection and diffusion, if a passive tracer is non-zero, the mean age concentration increases in time, and $\frac{da(\boldsymbol{x},t)}{dt} = 1$.

In the present study, the first term on the right-hand side of equation (6) was added to the ROMS code, and equations (5) and (6) were solved together numerically. Here, we regard locations where the concentration is lower than 10^{-4} as being free of SFB plume water, and water age there is undefined. The initial conditions for both C and α is zero.

5.2 Surface Mean Age of the SFB Plume

Figure 13*a* shows the two-year averaged surface mean age. Water age increases rapidly with increasing radius from the Golden Gate; starting at 0 days, up to roughly 20 days at a distance of 20 km from the Golden Gate. Within the main body of the plume ($C_{VI} \geq 0.1$; encompassed by the dashed line in Figures 7*b* and 13*a*), the average surface mean age ranges from 0–45 days. The maximum value of surface mean age in the Gulf of the Farallones is around 50 days, which indicates that the SFB-sourced water is typically flushed out of the region within this time frame. Consistent with the three-pathway pattern of baywater

dispersal described in section 4, we see the farthest penetration of young water along the coast north of the Golden Gate. For example, water with a mean age of 45 days can be found 120 km up the northern coast. Water in Drakes Bay is persistently freshened as it retains SFB-sourced water, and the mean age there ranges between 20–25 days. On the other hand, along the southern coast, water with a mean age of 45 days only extends up to 90 km from the Golden Gate. Half Moon Bay experiences slightly older water than just offshore, and Monterey Bay hosts relatively old water with mean age of 55–60 days when the plume travels far enough south.

Temporal variability is highlighted when considering monthly averaged surface mean age as shown in Figures 13b–m (c.f., passive tracer concentrations in Figures 7d–o). In some months, water is transported more rapidly through the Gulf, with surface mean ages less than 30 days throughout much of the region (e.g., June). On the other hand, there are months where water is retained for much longer time periods within the Gulf. April shows the oldest average age in the Gulf of the Farallones, that is, around 60–70 days. The mean age is inversely related to the baywater discharge (more rapid flushing associated with stronger outflow). Mean age north of the Golden Gate decreases during northward surface transport of young water directly from the Golden Gate (often associated with southerly winds), and increases during southward transport (often associated with northerly winds). Overall, the cross-shore distribution of surface mean age in Figure 13 echoes the baywater dispersal pattern shown in Figure 7 (i.e., the portion of the southern shelf occupied by young water is wider and shifted offshore more than that of the northern shelf due to the differential Ekman transports).

6 Summary and Discussion

We conducted a study of the dispersal of the San Francisco Bay plume over the northern and central California shelf. Two years (2011–2012) of high-resolution simulations were used to analyze the baywater dispersal pathways and associated time scales (i.e., mean water age) in terms of both mean behaviour and temporal variability. High-frequency ocean-bay exchange data that are available from an existing estuarine model (SCHISM) were applied to the domain's eastern boundary at the Golden Gate through which the SFB-sourced water enters the coastal ocean. A passive tracer was introduced to facilitate an unambiguous measure of the baywater dispersal.

Tidal forcing is an important factor in driving exchange at the Golden Gate (e.g., Fram et al., 2007) as well as mixing (e.g., MacCready et al., 2009, as in the Columbia River plume), particularly within the estuary. Previous work has also shown that tides exert an important influence at the inflow of a buoyant plume over one tidal cycle (McCabe et al., 2009) and can enhance cross-shelf mixing in the absence of other forcing (e.g., Izett & Fennel, 2018a). We did not carry out analysis of mixing associated with tidal bottom stresses along the shelf but generally find that the plume structure is surface enhanced except for a narrow region immediately outside the Golden Gate. Thus while tidal motion is critical in that vicinity, plume variability is largely dominated by wind stress forcing.

In spite of the complex coastline of the region, the San Francisco Bay plume behaves similarly to other river-sourced buoyant plumes, including idealized plumes. Upon entering the ocean, the vast majority of the SFB plume is sharply differentiated from the underlying shelf water. We identify three distinct transport pathways: a southward pathway that extends 80 km south of the Golden Gate on average; a northward pathway that reaches as far as 120 km north of the Golden Gate on average; and an offshore pathway that transiently delivers baywater cross-shore, which largely ceases near the shelf break (Figure 7). The natural tendency for the plume to turn north under the influence of the Coriolis force, combined with northward surface currents during downwelling conditions, result in a plume that is narrower and deeper in Figures 7 and 11 (e.g., Fong & Geyer, 2002; Lv et al., 2020; Izett & Fennel, 2018a) compared to the southern branch which is favored during upwelling conditions that result in a broader, shallower plume (as in Fong & Geyer, 2001, 2002). Though intra- and inter-annual variability exists, shelf waters within the Gulf of the Farallones exhibit water ages typically less than 50 days from release at the Golden Gate.

Overall, we find similar behavior to the Columbia River plume described by Hickey et al. (2005). As with our analysis, they find that a bi-directional plume is present at the Columbia River outflow due to the presence of both upwelling and downwelling wind conditions. The narrower northward branch of the Columbia River plume occurs roughly 50% of the time, which is similar to the 42% we find for the SF Bay plume. Despite its less frequent occurrence (26% of the time), the southern pathway contributes most to export (35.1% of total baywater) due to the coincidence of high plume discharge and northerly winds in Spring 2011. Wind forcing is the dominant factor in determining the prevailing direction of the plume, with a lag of three days between a weakening or reversal of winds

and a reversal of plume direction. This value is consistent with Hickey et al. (2005) who also find a lag with wind reversal and a propagation of the plume front of roughly 35 km d^{-1}.

The dispersal pathways of the plume have implications for biogeochemical processes over northern and central California shelf because the San Francisco Bay is a significant source of nutrients, organic matter, and dissolved and suspended contaminants to the shelf, with loads similar to open ocean inputs (Hurst & Bruland, 2008). The patterns of baywater dispersal revealed here indicate that the destination of material transported in the San Francisco Bay discharge changes rapidly on the scales of a few days, but also with longer-term seasonal differences. The water age analysis echoes the pattern of tracer dispersal pathways, with youngest water near the Golden Gate (<10 days old) and within the main body of the plume (< 50 days on average). For river-borne material that is biologically or geochemically active on time scales from a few days to months, the transport pathways and water age inferred here will influence deposition, availability to the regional marine ecosystem in several national marine sanctuaries (e.g., the Gulf of the Farallones NMS, the Cordell Bank NMS, and the Monterey Bay NMS), as well as regions where material may be exported from the San Francisco Bay by advection. When considering export timescales, a change of just a few days can have a significant impact on the amount of nutrients processed locally or downstream within a plume (Izett & Fennel, 2018b). Similar to the work by Kessouri et al. (2021), follow-up work should use physical-biogeochemical coupled simulations to explore the importance of anthropogenic nutrient loads in the California Current System, which is one of the world's four major wind-driven upwelling systems.

Data Availability Statement

The model code and outputs of this study are available at: https://doi.org/10.5281/zenodo.7433924.

Acknowledgments

This work was funded by the San Francisco Estuary Institute (SFEI) grant #1270, the California Ocean Protection Council grant #17661, the National Natural Science Foundation of China (52209085), the Jiangsu Specially-Appointed Professor Program (B1203512), and the Fundamental Research Funds for the Central Universities (B220201033). Computational resources were provided by the Extreme Science and Engineering Discovery Environment (XSEDE) through allocations TG-OCE170017 and TG-OCE030000N. We thank Zhengui Wang and Fei Chai for sharing the SCHISM data of high-frequency ocean-estuary exchanges.

References

Basdurak, N. B., Largier, J. L., & Nidzieko, N. J. (2020). Modeling the dynamics of small-scale river and creek plumes in tidal waters. *Journal of Geophysical Research: Oceans*, *125*, e2019JC015737.

Brink, K. H. (1998). Deep sea forcing and exchange processes. In K. H. Brink & A. R. Robinson (Eds.), *The global coastal ocean: process and methods* (Vol. 10, p. 151-167). Cambridge, MA: Harvard University Press.

Cahill, B., Schofield, O., Chant, R., Wilkin, J., Hunter, E., Glenn, S., & Bissett, P. (2008). Dynamics of turbid buoyant plumes and the feedbacks on near-shore biogeochemistry and physics. *Geophysical Research Letters*, *35*, L10605.

Carslaw, H. S., & Jaeger, J. C. (1959). *Conduction of heat in solids.* New York: Oxford University Press. (520 pp)

Castelao, R., Schofield, O., Glenn, S., Chant, R., & Kohut, J. (2008). Cross-shelf transport of freshwater on the New Jersey shelf. *Journal of Geophysical Research: Oceans*, *113*, C07017.

Chin, J. L., Ueber, E., Stauffer, P. H., & James W. Hendley II. (2001). *Beyond the golden gate; oceanography, geology, biology, and environmental issues in the gulf of the farallones* (Tech. Rep. No. 1198). USGS.

Cloern, J. E. (1996). Phytoplankton bloom dynamics in coastal ecosystems: A review with some general lessons from sustained investigation of San Francisco Bay, California. *Reviews of Geophysics*, *34*, 127-168.

Cloern, J. E., Schraga, T. S., Nejad, E., & Martin, C. (2020). Nutrient status of San Francisco Bay and its management implications. *Estuaries and Coasts*, *43*, 1299-1317.

Connolly, T. P., Hickey, B. M., Shulman, I., & Thomson, R. E. (2014). Coastal trapped waves, alongshore pressure gradients, and the California Undercurrent. *Journal of Physical Oceanography*, *44(1)*, 319-342.

Crank, J. (1975). *The mathematics of diffusion.* London, WI: Oxford University Press. (414 pp)

Delhez, E. J. M., Campin, J., Hirst, A. C., & Deleersnijder, E. (1999). Toward a general theory of the age in ocean modeling. *Ocean Modelling*, *1*, 17-27.

Deutsch, C., Frenzel, H., McWilliams, J. C., Renault, L., Kessouri, F., Howard, E., ... Yang, S. (2020). Biogeochemical variability in the California Current System. *bioRxiv*, *2(10)*,

673 942565.

674 Egbert, G. D., & Erofeeva, S. Y. (2002). Efficient inverse modeling of barotropic ocean
675 tides. *Journal of Atmospheric and Oceanic Technology*, *19*(2), 183-204.

676 Fong, D. A., & Geyer, W. R. (2001). Response of a river plume during an upwelling favorable
677 wind event. *Journal of Geophysical Research: Oceans*, *106(C1)*, 1067-1084.

678 Fong, D. A., & Geyer, W. R. (2002). The alongshore transport of freshwater in a surface-
679 trapped river plume. *Journal of Physical Oceanography*, *32*, 957-972.

680 Fram, J. P., Martin, M. A., & Stacey, M. T. (2007). Dispersive fluxes between the coastal
681 ocean and a semienclosed estuarine basin. *Journal of Physical Oceanography*, *37*,
682 1645-1660.

683 Garvine, R. W. (1999). Penetration of buoyant coastal discharge onto the continental shelf:
684 A numerical model experiment. *Journal of Physical Oceanography*, *29*, 1892-1909.

685 Geyer, W. R., & MacCready, P. (2014). The estuarine circulation. *Annual Review of Fluid*
686 *Mechanics*, *46*, 175-197.

687 Godin, G. (1972). *The analysis of tides*. Toronto: University of Toronto Press. (264 pp)

688 Gruber, N., Lachkar, Z., Frenzel, H., Marchesiello, P., Munnich, M., McWilliams, J., ...
689 Plattner, G.-K. (2011). Eddy-induced reduction of biological production in eastern
690 boundary upwelling systems. *Nature Geosciences*, *4*, 787–792.

691 Hickey, B. M. (1998). Coastal oceanography of Western North America from the tip of
692 Baja California to Vancouver Island. In K. H. Brink & A. R. Robinson (Eds.), *The*
693 *Sea* (Vol. 11, p. 345-393). New York, NY: Wiley and Sons, Inc.

694 Hickey, B. M., Geier, S., Kachel, N., & MacFadyen, A. (2005). A bi-directional river plume:
695 The columbia in summer. *Continental Shelf Research*, *25*(14), 1631-1656.

696 Hickey, B. M., & Pola, N. E. (1983). The seasonal alongshore pressure gradient on the
697 West Coast of the United States. *Journal of Geophysical Research: Oceans*, *88(C12)*,
698 7623-7633.

699 Horner-Devine, A. R., Hetland, R. D., & MacDonald, D. G. (2015). Mixing and transport
700 in coastal river plumes. *Annual Review of Fluid Mechanics*, *47*, 569-594.

701 Hurst, M. P., & Bruland, K. W. (2008). The effects of the San Francisco Bay plume on
702 tracer metal and nutrient distributions in the Gulf of the Farallones. *Geochimica et*
703 *Cosmochimica Acta*, *72*, 395-411.

704 Huyer, A. (1983). Coastal upwelling in the california current system. *Progress in Oceanog-*
705 *raphy*, *12*(3), 259-284.

Izett, J. G., & Fennel, K. (2018a). Estimating the cross-shelf export of riverine materials: Part 1. general relationships from an idealized numerical model. *Global Biogeochemical Cycles*, *32*(2), 160-175.

Izett, J. G., & Fennel, K. (2018b). Estimating the cross-shelf export of riverine materials: Part 2. estimates of global freshwater and nutrient export. *Global Biogeochemical Cycles*, *32*(2), 176-186.

Jacox, M. G., Edwards, C. A., Hazen, E. L., & Bograd, S. J. (2018). Coastal upwelling revisited: Ekman, Bakun, and improved upwelling indices for the U.S. West Coast. *Journal of Geophysical Research: Oceans*, *123*, 7332-7350.

Kaplan, D. M., & Largier, J. (2006). HF radar-derived origin and destination of surface waters off Bodega Bay, California. *Deep Sea Research Part II: Topical Studies in Oceanography*, *53*, 2906-2930.

Kessouri, F., Bianchi, D., Renault, L., McWilliams, J. C., Frenzel, H., & Deutsch, C. A. (2020). Submesoscale currents modulate the seasonal cycle of nutrients and productivity in the California Current System. *Global Biogeochemical Cycles*, *34*, e2020GB006578.

Kessouri, F., McLaughlin, K., Sutula, M., Bianchi, D., Ho, M., McWilliams, J. C., ... Leinweber, A. (2020). Configuration and validation of an oceanic physical and biogeochemical model to investigate coastal eutrophication in the Southern California Bight. *Earth and Space Science Open Archive*, 1-62.

Kessouri, F., McWilliams, J. C., Bianchi, D., Sutula, M., Renault, L., Deutsch, C., ... Weisberg, S. B. (2021). Coastal eutrophication drives acidification, oxygen loss, and ecosystem change in a major oceanic upwelling system. *Proceedings of the National Academy of Sciences*, *118*(21), e2018856118.

Large, W. G., McWilliams, J. C., & Doney, S. C. (1994). Oceanic vertical mixing: A review and a model with a nonlocal buoyancy layer parameterization. *Reviews of Geophysics*, *32(4)*, 363-403.

Lentz, S. (2004). The response of buoyant coastal plumes to upwelling-favorable winds. *Journal of Physical Oceanography*, *34*, 2458-2469.

Lentz, S. J. (1987). A description of the 1981 and 1982 soring transition over the northern california shelf. *Journal of Geophysical Research: Oceans*, *92*, 1545-1567.

Lv, R., Cheng, P., & Gan, J. (2020). Adjustment of river plume fronts during downwelling-favorable wind events. *Continental Shelf Research*, *202*, 104143.

MacCready, P., Banas, N. S., Hickey, B. M., Dever, E. P., & Liu, Y. (2009). A model study of tide- and wind-induced mixing in the columbia river estuary and plume. *Continental Shelf Research*, *29*(1), 278-291.

Marchesiello, P., McWilliams, J. C., & Shchepetkin, A. (2001). Open boundary conditions for long-term integration of regional oceanic models. *Ocean Modelling*, *3(1-2)*, 1-20.

Marchesiello, P., McWilliams, J. C., & Shchepetkin, A. (2003). Equilibrium structure and dynamics of the California Current System. *Journal of Physical Oceanography*, *33*, 753-783.

Mason, E., Molemaker, J., Shchepetkin, A. F., Colas, F., McWilliams, J. C., & Sangra, P. (2010). Procedures for offline grid nesting in regional ocean models. *Ocean Modelling*, *35(1-2)*, 1-15.

McCabe, R. M., MacCready, P., & Hickey, B. M. (2009). Ebb-tide dynamics and spreading of a large river plume. *Journal of Physical Oceanography*, *39*(11), 2839 - 2856.

Reid, J. L., & Schwartzlose, R. A. (1962). Direct measurements of the Davidson Current off central California. *Journal of Geophysical Research: Oceans*, *67(6)*, 2491-2497.

Renault, L., Hall, A., & McWilliams, J. C. (2016). Orographic shaping of u.s. west coast wind profiles during the upwelling season. *Climate Dynamics*, *46*, 273-289.

Renault, L., McWilliams, J. C., Jousse, A., Deutsch, C., Frenzel, H., Kessouri, F., & Chen, R. (2020). The physical structure and behavior of the California Current System. *bioRxiv*, *2(10)*, 942730.

Renault, L., Molemaker, M. L., McWilliams, J. C., Shchepetkin, A. F., Lemarie, F., Chelton, D., ... Hall, A. (2016). Modulation of wind work by oceanic current interaction with the atmosphere. *Journal of Physical Oceanography*, *46*, 1685-1704.

Sharples, J., Middelburg, J. J., Fennel, K., & Jickells, T. D. (2017). What proportion of riverine nutrients reaches the open ocean? *Global Biogeochemical Cycles*, *31*.

Shchepetkin, A. F. (2015). An adaptive, courant-number-dependent implicit scheme for vertical advection in oceanic modeling. *Ocean Modelling*, *91*, 38-69.

Shchepetkin, A. F., & McWilliams, J. C. (2005). The Regional Oceanic Modeling System (ROMS): A split-explicit, free-surface, topography-following-coordinate oceanic model. *Ocean Modelling*, *9(4)*, 347-404.

Shchepetkin, A. F., & McWilliams, J. C. (2009). Correction and commentary for "Ocean forcasting in terrain-following coordinates: Formulation and skill assessment of the regional ocean modeling system" by Haidvogel et al. J. Comp. Phys. 227, pp. 3595-

3624. *Journal of Computational Physics*, *228(24)*, 8985-9000.

Trenberth, K. E., Smith, L., Qian, T., Dai, A., & Fasullo, J. (2007). Estimates of the global water budget and its annual cycle using observational and model data. *Journal of Hydrometeorology*, *8*, 758-769.

Wang, Z., Chai, F., Dugdale, R., Liu, Q., Xue, H., Wilkerson, F., ... Zhang, H. (2020). The interannual variabilities of chlorophyll and nutrients in San Francisco Bay: a modeling study. *Ocean Dynamics*, *70*, 1169-1186.

Whitney, M. M., & Garvine, R. W. (2006). Simulating the Delaware Bay buoyant outflow: Comparison with observations. *Journal of Physical Oceanography*, *36*, 3-21.

Xiao, C., Zhang, W., & Chen, Y. (2021). Impact of shelf valleys on the spread of surface-trapped river plumes. *Journal of Physical Oceanography*, *51*, 247-266.

Zhang, W. G., Wilkin, J. L., & Schofield, O. M. E. (2010). Simulation of water age and residence time in New York Bight. *Journal of Physical Oceanography*, *40*, 965-982.

Zhang, Y., & Baptista, A. M. (2008). SFLFE: A semi-implicit Eulerian-Lagrangian finite-element model for cross-scale ocean circulation. *Ocean Modelling*, *21(3-4)*, 71-96.

Zhang, Y., Ye, F., Stanev, E. V., & Grashorn, S. (2016). Seamless cross-scale modeling with SCHISM. *Ocean Modelling*, *102*, 64-81.

Zhou, J., & Stacey, M. T. (2020). Residual sediment transport in tidally energetic estuarine channels with lateral bathymetric variation. *Journal of Geophysical Research: Oceans*, *125*, e2020JC016140.

Zhou, J., Stacey, M. T., Holleman, R. C., Nuss, E., & Senn, D. B. (2020). Numerical investigation of baroclinic channel-shoal interaction in partially stratified estuaries. *Journal of Geophysical Research: Oceans*, *125*, e2020JC016135.